This is a repository copy of *Perovskite crystallization dynamics during spin-casting : an In situ wide-angle x-ray scattering study*.

White Rose Research Online URL for this paper:
http://eprints.whiterose.ac.uk/163831/

Version: Published Version

Article

Perovskite Crystallization Dynamics during Spin-Casting: An *In Situ* Wide-Angle X-ray Scattering Study

Noura Alhazmi, Edwin Pineda, Jonathan Rawle, Jonathan R. Howse, and Alan D. F. Dunbar*

Cite This: *ACS Appl. Energy Mater.* 2020, 3, 6155–6164

Read Online

ACCESS | Metrics & More | Article Recommendations | Supporting Information

ABSTRACT: *In situ* wide-angle X-ray scattering (WAXS) has been measured during the spin coating process used to make the precursor films required for the formation of thin films of perovskite. A customized hollow axis spin coater was developed to permit the scattered X-rays to be collected in transmission geometry during the deposition process. Spin coating is the technique most commonly used in laboratories to make thin perovskite films. The dynamics of spin-casting $MAPbI_{3-x}Cl_x$ and $FAPbI_{3-x}Cl_x$ films have been investigated and compared to investigate the differences between the dynamics of $MAPbI_{3-x}Cl_x$ and $FAPbI_{3-x}Cl_x$ film formation. In particular, we focus on the crystallization dynamics of the precursor film formation. When casting $MAPbI_{3-x}Cl_x$, we observed relatively fast 1D crystallization of the intermediate product MA_2PbI_3Cl. There was an absence of the desired perovskite phase formed directly; it only appeared after an annealing step that converted the MA_2PbI_3Cl to $MAPbI_3$. In contrast, slower crystallization via a 3D precursor was observed for $FAPbI_{3-x}Cl_x$ film formation compared to $MAPbI_{3-x}Cl_x$. Another important finding was that some $FAPbI_{3-x}Cl_x$ perovskite was generated directly during spin-casting before annealing. These findings indicate that there are significant differences between the crystallization pathways for these two perovskite materials. These are likely to explain the differences in the lifetimes of the resulting perovskite solar cell devices produced using FA and MA cations.

KEYWORDS: *perovskite, wide-angle X-ray scattering, crystallization, spin coating, dynamics*
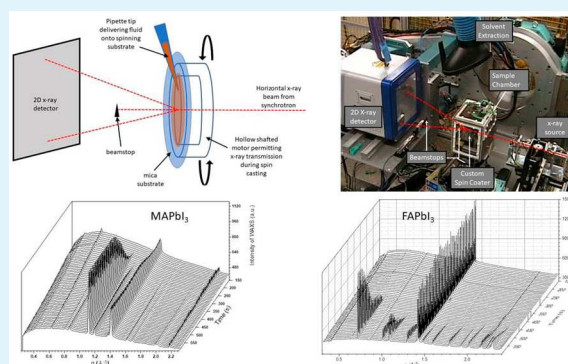
1. INTRODUCTION

Hybrid organic–inorganic perovskites have received a great deal of attention as materials for the next generation of solar technology. They are attractive due to their high power conversion efficiency (PCE), low cost, and ease of fabrication when compared to other solar cell materials. They have remarkable defect tolerance, resulting in high-performance devices produced from relatively crude processing techniques.[1] The power conversion efficiency of perovskite devices has increased rapidly jumping from 3.8% in 2009[2] to more than 25.2% efficiency recorded in 2017.[3] However, they are yet to become widely available commercially with limitations including perovskite decomposition in air and concerns about toxicity of the lead. The performance of the devices is inextricably linked to properties of the films formed such as their morphology, coverage, and conformity to the underlying substrate.[4,5] Therefore, there is a definite need for a deep understanding of the dynamics of crystal formation during film processing to ensure that the crystal growth can predictably be controlled, because the thermodynamic stability and/or the presence of defects within the final films produced will have a profound effect upon on the performance of the resulting devices. Methylammonium lead iodide ($MAPbI_3$) has emerged as one of the most popular perovskites to study. It is often

formed from a 3:1 $MAI/PbCl_2$ solution, where the Cl ions play a role in controlling the crystallization of the perovskite.[6−10] $MAPbI_3$ formation is achieved by spin-casting, during which time the solution (which may already contain isolated precursor crystals[11]) dries to leave a film of precursor material. This precursor material is a mixture primarily composed of $MA_2PbI_3Cl(s)$ + MACl(amorphous) and upon annealing is converted to $MAPbI_3$ as the MACl sublimes[12] into the surrounding atmosphere (with the amorphous MACl subliming before the MACl produced as the MA_2PbI_3Cl decomposes[8]). There have been many *ex situ* X-ray scattering studies of perovskite films, which have helped to determine the final crystal structures and crystallite size distribution; however, in order to obtain a greater understanding of the crystallization processes themselves, it is necessary to study the process *in situ*.
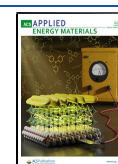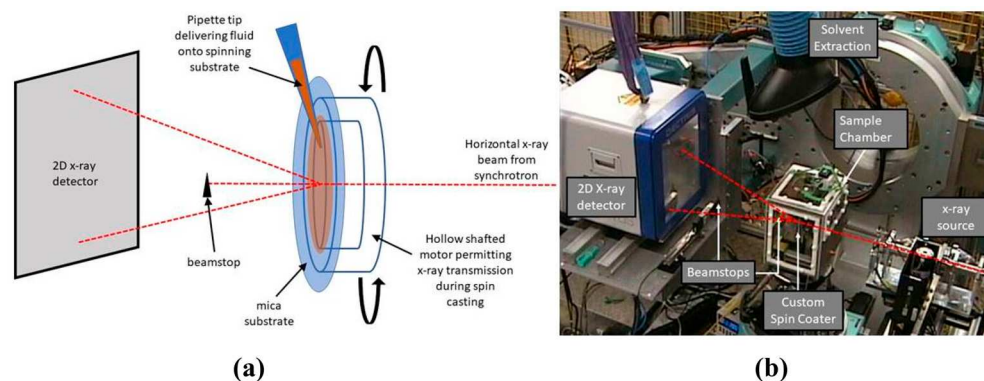
Figure 1. Setup used for the *in situ* WAXS experiments. The schematic view of the transmission geometry is illustrated in (a), while the photograph of the setup at i07 is shown in (b), including the end of the X-ray pipe at the synchrotron, the sample chamber and the 2D X-ray detector.

Several studies have focused on the dynamics of the precursor conversion to perovskite. Chang et al. studied the formation mechanism of MAPbI$_3$ film prepared by drop-casting onto a substrate at temperatures between 70 and 180 °C using *in situ* X-ray scattering.[13] Their findings indicate that the perovskite formation varies with substrate temperature, and direct formation of the MAPbI$_3$ perovskite is associated with substrate temperatures of 140 °C and higher. Similar *in situ* methods have been applied to track the latter stages of MAPbI$_3$ formation during annealing of precursor films preprepared by spin coating.[13−15] The highly crystallized perovskite films were observed to form during thermal annealing at a temperature of 80 °C. Annealing times of more than 1 h at 80 °C resulted in films which when incorporated in devices achieve a PCE of 12%.[14] Moore et al. used X-ray scattering to study the crystallization kinetics of organic−inorganic trihalide perovskites, finding that the primary step in perovskite formation is removal of excess organic salt from the precursor, which led them to propose that careful choice of the lead salt will aid in controlling crystal growth.[16] They also made films using different solvents and found little difference in the perovskites formed and therefore discerned that the solvent was not incorporated within the crystal structure of the precursor films, although their TGA data indicated some residual solvent remained in the films. They also noted that a high degree of orientation of the films formed in the direction normal to the substrate. Lilliu et al. also utilized the grazing incidence geometry to study crystallization in MAPbI$_{3−x}$Cl$_x$.[17] They observed a slight rotation as well as an expansion or contraction of some of the precursor and perovskite crystallites upon annealing. Alsari et al. used in operando measurements of interdigitated back contact solar cells to demonstrate that the precursor film converts into perovskite with a well-defined band gap early in the transformation, highlighting the remarkable defect tolerance of these materials.[1] The photovoltage peaks early, when only a fraction of the precursor has been converted to perovskite, presumably due to the photovoltaic effect occurring in a limited number of isolated crystals. This photovoltage then drops slightly as the conversion completes, which they attribute to induced strain and defects at grain boundaries. Stone et al. revealed the structure of the precursor material.[8] They found that the precursor film contains 1D chains of MA$_2$PbI$_3$Cl coexisting with disordered MACl. This precursor forms a continuous film free of pinholes. The disordered MACl present dramatically hinders the formation of the perovskite, because upon

annealing, the disordered MACl must first evaporate before the MA$_2$PbI$_3$Cl converts to MAPbI$_3$ and yet more MACl, which is liberated as a gas. The time taken for the disordered MACl to evaporate slows the conversion process, allowing the pinhole free morphology to be retained. If the annealing process for either MA or FA perovskites proceeds for too long, the perovskite subsequently degrades into PbI$_2$.[16,18] Understanding of the precursor film to perovskite has been improved significantly by these *in situ* studies. However, there is still a lack of understanding of the mechanisms that result in the formation of the original precursor films, which will clearly have a strong influence on the final film properties. This limits our ability to deliberately control the morphology of the films formed.

Munir et al. studied the precursor film formation. They used *in situ* grazing incidence wide-angle X-ray scattering to study the formation of MAPbI$_3$ during spin-casting.[7] They found that the amount of halide present influences the phase of the precursor and when MAI/PbCl$_2$ is used in a 3:1 ratio (as opposed to 1:1), substantially more solvent is retained in the film. The extra MAI alters the solidification process, resulting in a slower drying process and a less ordered and less stable precursor film that upon annealing loses significant mass, which they attributed to solvent drying.

Here, we focus on the dynamics of the precursor formation. We study the early stages of the process *in situ* during the spin coating to produce the precursor films before thermal annealing in air. We focus primarily on the formation of MAPbI$_3$ from a 3:1 mixed solution of MAI/PbCl$_2$ in dimethylformamide (DMF), and we subsequently compare the results to the formation of FAPbI$_{3−x}$Cl$_x$ from a similar 3:1 mixed solution (in DMF) of FAI/PbCl$_2$. While this study focuses on perovskite film formation for solar cell applications, it should be noted that the experimental setup developed for this investigation could equally be used to study the spin-casting of other materials.

2. EXPERIMENTAL METHODS

2a. Perovskite Preparation. Two of the commonly investigated perovskite materials MAPbI$_3$ and FAPbI$_{3−x}$Cl$_x$ have been studied during spin-casting into thin films. The perovskite solutions used for the deposition were prepared following similar processes to those reported in the literature.[19−21] In brief, to prepare the casting solution for MAPbI$_3$, methylammonium iodide (MAI) and lead chloride (PbCl$_2$), purchased from Sigma-Aldrich and used without further purification, were mixed in a 3:1 molar ratio. The mixture was dissolved in anhydrous dimethylformamide (DMF), also purchased

from Sigma-Aldrich, to form a 3.2 M solution. Similarly, the casting solution for FAPbI$_{3-x}$Cl$_x$ was prepared by mixing formamidinium iodide (FAI), purchased from Ossila Ltd., and lead chloride (PbCl$_2$), purchased from Sigma-Aldrich, in the same 3:1 molar ratio. The mixture was then dissolved in anhydrous DMF to form a 3.2 M solution as reported in the literature.[22] In both cases, the solutions were heated for 30 min on a hot plate surface at 70 °C to ensure complete dissolution of the mixed powder products before deposition.

2b. In Situ WAXS Experimental Setup. 2D WAXS images from the perovskite solution and crystalline film were measured *in situ* during the spin-casting process. Mica sheets of 1 × 1 cm^2 were used as the substrate for these measurements, because mica is known to be largely X-ray transparent with on a few scattering spots associated with its crystalline structure. It was assumed that the crystallization that occurs when spin-casting on mica would be similar to casting on more conventional substrates; this assumption was supported by the similar morphologies observed by SEM and similar optical absorbance properties. A substrate was mounted on the custom-built spin coater, shown in Figure 1, which had a hollow shaft to permit X-ray transmission through the substrate and sample during the solution-casting process. The spin coater was oriented such that its rotation occurs in a vertical plane perpendicular to the incident X-ray beam, which was horizontal approximately along the axis of rotation. A spin speed of 1660 rpm was used. Rotating the substrate in a vertical plane has the advantage of making alignment of the X-ray beam to the sample very simple. The X-ray beam was perpendicular to the substrate surface and therefore was sensitive to ordering along the plane of the sample but may not pick up ordering out of plane, i.e., planes parallel to the surface of the sample. This is not an issue assuming the samples are isotropic but should be kept in mind for highly oriented films. The solution to be cast was pipetted onto the substrate surface above the measurement point, and while it was running down the static substrate, the spinning process and data collection were initiated. Therefore, this restricted the spin coating process to only a small area. The spin coater was housed inside a custom-built chamber in front of a beamstop and after a series of slits to reduce background scatter and also as a safety measure to ensure solvent vapor was extracted by the ventilation system. The chamber was filled with He to further minimize background scatter due to air scattering the intense X-ray beams. A 100 μL aliquot of perovskite solution was loaded into a pipet tip using a syringe pump, which was controlled remotely due to the ionizing radiation needed for the X-ray experiment. The solution was then deposited into a substrate mounted on the hollow of the shaft motor. Once the solution was deposited onto the substrate surface, the rotation and the X-ray measurements were started. The high flux of X-ray synchrotron radiation available at Beamline i07 at the Diamond Light Source (Didcot, England) was used as the X-ray source. The X-ray energy was 10.5 keV corresponding to a wavelength of 1.18 Å. The beam resulted in a spot size on the sample that was approximately 100 μm high by 200 μm wide. The 2D WAXS images were recorded using a Pilatus 2 M detector at a distance of 42.1 cm from the sample. The experimental setup was calibrated by measuring a sample of silver behenate, which has a well-defined structure.[23,24] For image processing and data analysis, the software package DAWN was used.[25] Fast 2D images with an integration time of 0.5 s were saved over the first 150 s, followed by slower images with better statistics due to an integration time of 5 s per image. For each of these images, the data transfer took 2.8 s, resulting in one profile every 7.8 s. The total measurement time was approximately 600 s. The fast data sets did not show anything other than a reduction in the solvent scattering; therefore, only the slow data sets are presented here. Unlike the other works in the literature that use the grazing incidence geometry for their experiments, in this work, transmission geometry with the substrate mounted vertically is used instead. This approach has the advantage of being very simple to align experimentally, does not suffer from sample misalignment during deposition, and because the sample precesses through the beam, sample damage is minimized. When the sample was static, only a few discrete spots were observed in the 2D WAXS images, indicating that a small number of crystallites

were being probed. However, when spinning a circle of the sample is passed through the beam (because of an intentional misalignment of the center of rotation of the spin coater and the beam path—typically about 2 mm), this "spottiness" is averaged out, resulting in a more even distribution of scattering around the rings in the 2D WAXS images, as shown in Figures S3 and S5. A spinning experiment probes a much larger number of crystallites than a static experiment. Any beam damage caused by the X-rays was minimized by this movement of the sample through the beam and the use of a fast shutter to limit the exposure to the minimum time required for the measurements to be made. Ideally, the annealing process would also be done *in situ* also, but the setup developed did not permit this. This is an area for future experimental development.

After casting, the films were removed from the spin coater and annealed in keeping with typical processes used in the literature.[14] The MAPbI$_3$ films were annealed on a hot plate at 90 °C for 2 h, whereas the FAPbI$_{3-x}$Cl$_x$ films were annealed on a hot plate at 190 °C for 1 h. The temperatures reported are the temperature of the hot plate surface rather than the sample surface; measurements on similar samples suggest this overestimates the sample surface temperature by about 10 °C. The samples were then returned to the sample environment and a 2D WAXS image collected as described above.

3. RESULTS AND DISCUSSION

### 3a. In Situ Spin Coating of the 3:1 MAI:PbCl$_2$ Solution.
Figure 2 shows the 1D radially integrated scattering intensity
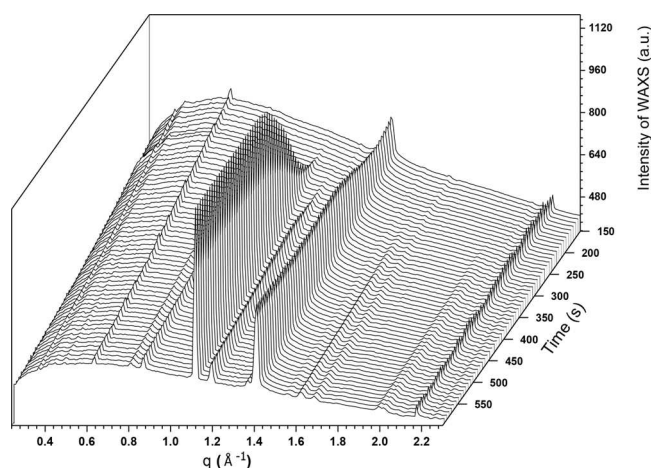
Figure 2. 1D integrated radial profile of the WAXS generated showing the formation of the precursor MA$_2$PbI$_3$Cl during the spin-casting of 3:1 MAI/PbCl$_2$ solution plotted as a function of time.

profiles, which were generated from the 2D images collected during the *in situ* spin coating of the 3:1 MAI/PbCl$_2$ solution to form a film of the MA$_2$PbI$_3$Cl precursor. Throughout the process, peaks associated with the mica substrate were observed at 1.4 and 2.16 Å^{-1} as is indicated in the Supporting Information in Figure S1.
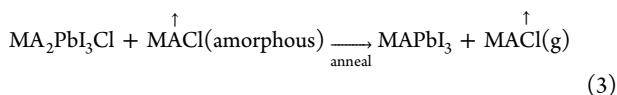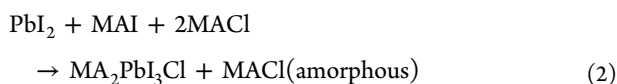
At the start of the process, the mica feature is superimposed on a broad scattering feature, which is most intense between 0.4 and 1.2 Å^{-1}. This broad feature is attributed to scattering due to the solvent as has previously been proposed.[12,17] In the initial seconds, the film thinning process will be dominated by rapid liquid loss due to radial flow, and then, in latter stages, it is dominated by solvent evaporation. As time progresses, the solvent feature reduces in intensity as expected, and other peaks associated with the formation of crystals of intermediate products are observed in the *in situ* WAXS data. The peak at q = 1.1 Å^{-1} has been generally assigned to a perovskite precursor phase, as was previously reported in other WAXS studies.[8,26,27]

(a)   (b)
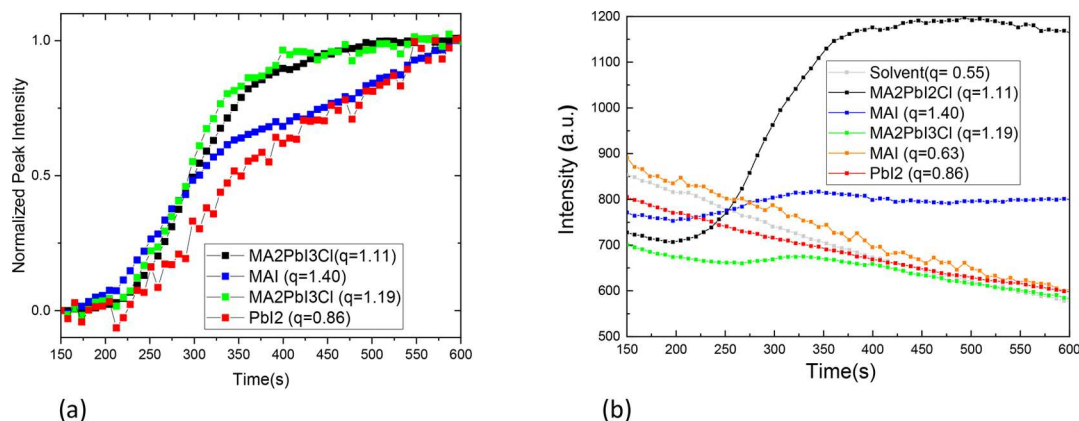
Figure 3. Intensity of the main WAXS features for the MA_2PbI_3Cl films as a function of time. Figure 3(a) is the peak intensity as measured, and Figure 3(b) is the same data set after normalization and correction for the reduction in the solvent background over time. The peak intensity of the solvent background scattering was taken at $q = 0.55$ Å^{-1}, MA_2PbI_3Cl was taken at $q = 1.11$ and 1.19 Å^{-1}, MAI was taken at $q = 0.63$ and 1.4 Å^{-1}, and the PbI_2 was taken at $q = 0.86$ Å^{-1}.

A similar peak was detected and defined more precisely as an intermediate product by Unger et al.,[28] Chun-Yu Chang et al.,[29] and Hui Yu et al.[19] in XRD measurements. Their studies highlighted a strong diffraction peak at a Bragg diffraction angle of 15.7°, which is equivalent to a scattering vector value of $q = 1.1$ Å^{-1} as calculated using $q = \left(\frac{2\pi}{d}\right) = \left(\frac{4\pi\sin\theta}{\lambda}\right)$ where the X-ray wavelength was assumed to be the Cu Kα wavelength $\lambda = 1.54$ Å.

Yu et al. proposed that the chemical reaction of 3 parts MAI with 1 part $PbCl_2$ produces several intermediate products, involving two reaction steps.[19] In the initial step, the MAI and $PbCl_2$ react to produce PbI_2, MAI, and MACl. This is followed by a reaction between PbI_2, MAI, and MACl to produce MA_2PbI_3Cl. Subsequently, upon heating, initially the amorphous MACl evaporates, and then, the precursor product decomposes to yield the perovskite product $MAPbI_3$ as well as MACl that is lost as a gas. These chemical reactions of 3:1 MAI with $PbCl_2$ are illustrated in the reaction eqs 1–3 below, taking into account the stoichiometry of the precursor and the annealing dynamics identified by Stone et al.[8] The structure of the precursor was determined to be 1D chains of lead halide octahedral with the equatorial sites on the chain populated exclusively by I. The precursor was identified as MA_2PbI_3Cl with some uncertainty in the halide stoichiometry coexisting with disordered MACl.

$$3MAI + PbCl_2 \rightarrow PbI_2 + MAI + 2MACl \qquad (1)$$

$$PbI_2 + MAI + 2MACl$$
$$\rightarrow MA_2PbI_3Cl + MACl(amorphous) \qquad (2)$$

$$MA_2PbI_3Cl + MACl(amorphous) \xrightarrow[anneal]{} MAPbI_3{\uparrow} + MACl(g){\uparrow}$$
$$\qquad (3)$$

In our *in situ* WAXS data during the casting of 3:1 MAI with $PbCl_2$, we observed a gradual increase in WAXS intensity around $q = 1.1$ Å^{-1} as shown in Figure 2, which is attributed to the formation of the intermediate phase of MA_2PbI_3Cl. As the thin film dries during the casting process, this scattering peak grows in intensity. The process results in the crystallization of an increasing amount of the intermediate product MA_2PbI_3Cl.

In addition to the peak at $q = 1.1$ Å^{-1}, the weaker scattering of X-ray peaks recorded at 1.19, 1.6, 1.7, and 2.0 Å^{-1} are also attributed to the MA_2PbI_3Cl intermediate product.[29,30] The positions of these scattering peaks are in agreement with experimental studies of the X-ray diffraction analysis[20,31] and with the modeling work reported in ref 32.

Sharp features at $q = 0.63$ Å^{-1}, $q = 1.40$ Å^{-1}, and around $q = 2.15$ Å^{-1} are attributed to crystallites of excess MAI, in agreement with peak positions reported in an investigation of the crystal structure of MAI reported previously.[33] Note that the MAI scattering at 1.4 Å^{-1} coincides with mica related feature. In hindsight, a different choice of substrate would have made the data analysis simpler.

The strong WAXS peak attributed to the intermediate phase MA_2PbI_3Cl at 1.1 Å^{-1} becomes evident at $t = 210$ s. This indicates the crystallization of MA_2PbI_3Cl from solution at room temperature as the solvent evaporates. After rapid initial growth, the strong intensity at $q = 1.1$ Å^{-1} remains constant until the end of the *in situ* WAXS measurement.

The dynamic formation of the precursor MA_2PbI_3Cl during the spin coating data suggests that there are three stages in the process. Figure 3 shows the evolution of the WAXS peak intensities as a function of time for the solvent centered at $q = 0.55$ Å^{-1}, the intermediate product MA_2PbI_3Cl at $q = 1.1$ Å^{-1}, and the scattering from MAI and mica at 1.4 Å^{-1}. Figure 3(a) shows the as observed peak intensity for each of the features of interest, whereas Figure 3(b) shows the same data after normalization and correcting for the solvent loss by subtracting the initial solvent intensity at that q value scaled by the solvent evaporation profile at each time step. This data processing makes the changes due to the crystallization process more straightforward to interpret and enables the data to be fitted using the Johnson–Mehl–Avrami–Kolmogorov equation

$$y = 1 - \exp(-k(t - t_0)^n)$$

where t is time, t_0 is the start of the process being fitted, k is a time constant for the process, and n is the Avrami exponent, following similar analysis used in the literature.[34,35] This expression was originally developed to describe isothermal phase transitions in metals such as crystallization. It has since been applied to crystallization in many different situations. In this simple form, the derivation was premised upon assumptions that the nucleation of the crystallites occurs

homogeneously and randomly, the growth rate is not affected by the extent of crystallization and occurs equally in all directions. It is uncertain whether all of these requirements are met in the system being studied; therefore, in order to avoid over interpreting the results, they are primarily used to determine an accurate onset time "t_0", and the exponential factor "n" is taken only as a crude indication of high or low dimensionality.[36−38] During the first stage, up to approximately 210 s, the process is dominated by solvent loss. After that, crystallization of the intermediate product MA_2PbI_3Cl occurs. The maximum intensity of the intermediate product peak is reached after about 350 s. After this, there are no significant changes in the crystalline products. The similarity of the two growth profiles shown in Figure 3(b) attributed to the intermediate product provides confirmation that their peak assignment to the same structure is correct. The crystallization of the unreacted PbI_2 at 0.86 Å^{-1} and MAI at 1.4 Å^{-1} starts at approximately the same time as the intermediate product. This indicates that with the casting solution for MA_2PbI_3Cl, the early stages of spin-casting are critical during the crystallization of perovskite films, with all the materials drying out of solution at the same time locking in the morphology of the final film.

As shown in Figure 4, the fitted Avrami exponent n is found to be 1.66 for the MA_2PbI_3Cl. This exponent is related to both
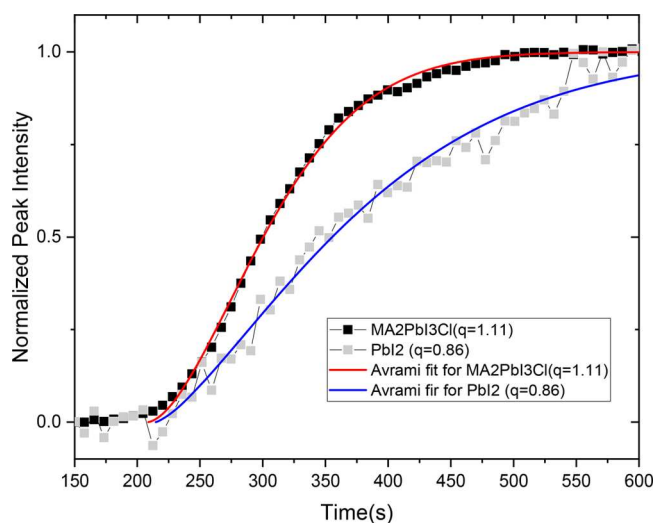
Figure 4. Avrami fitting applied to the WAXS peak intensity data for the formation of MA_2PbI_3Cl at q = 1.1 Å^{-1} and PbI_2 at q = 0.86 Å^{-1}. The Avrami exponent n was found to be 1.66 ± 0.09 for the MA_2PbI_3Cl and 1.37 ± 0.13 for the PbI_2; further details are shown in Figure S2.

the nature of the nucleation processes occurring and the dimensionality of the crystallization, and while it cannot be considered conclusive evidence, these results are consistent with low-dimensional growth. The structures of the MA_2PbI_3Cl chains formed are known to be one-dimensional.[8] This is consistent with 1D growth with some nucleation of 1D precursor crystals occurring. In comparison the PbI_2 exponent is even lower at 1.37, again suggesting low-dimensional growth for the PbI_2, perhaps with more limited nucleation and greater confinement between individual precursor crystals within the crystallizing layer. It should also be noted that the intensity of the PbI_2 peak is considerably weaker than that of the precursor peak. The onset time t_0 for the two fits are the same (within the margins of error at 209 ± 4 and 215 ± 11 s for the

MA_2PbI_3Cl and PbI_2, respectively), confirming the earlier assumption that they start at the same time.

It is noted that the onset of crystallization in our experimental setup is slower (precursor formation after 210 s) than that previously reported by Munir et al.[7] (precursor formation after 50 s). We attribute this to the slower spin speed used in our experiments (1660 as opposed to 2000 rpm) and the presence of an environmental chamber, which may slow the evaporation of the solvent due to a buildup of solvent vapor within the chamber. Therefore, we have inadvertently demonstrated that it is possible to control the crystallization dynamics. This control is promising, as it indicates that it is possible to change the crystallization dynamics and thereby optimize the morphology of the perovskite structures formed.

3b. WAXS from the MA_2PbI_3Cl Precursor Film upon Annealing. WAXS patterns from the MA_2PbI_3Cl precursor films were also measured before and after annealing to allow comparison between the as-cast and annealed samples. To achieve this, it was necessary to remove the as-cast samples from the horizontal axis spin coater and place them on a hot plate at the appropriate temperature. Once annealed for the desired time, the samples were replaced on the spin coater, and the corresponding WAXS pattern was recorded.

Figure 4 compares the 1D radially integrated WAXS profile for the as-cast dry film to the film after it has been annealed. The largest scattering peak in the as-cast precursor structure that was evident at 1.1 Å^{-1}, however, had almost entirely disappeared after the film was annealed. This indicates that this intermediate MA_2PbI_3Cl structure is thermally unstable and undergoes a transition to form the desired $MAPbI_3$ perovskite structure easily. The changes observed upon annealing the perovskite are attributed to a conversion occurring during thermal annealing as was explained in eq 3. During annealing, Lilliu et al.[17] observed orientation perturbations of both the MA_2PbI_3Cl and $MAPbI_3$ crystallites, which we attributed to the movement of the subliming MACl passing through the film to escape from the surface. In the annealed data set, there are new features not observed in the as-cast sample; in particular, there are strong peaks at q = 1.0 and 2.0 Å^{-1} attributed to the final $MAPbI_3$ perovskite structure, which has replaced the unstable intermediate phase. The peaks at q = 1.0 and 2.0 Å^{-1} are assigned to the (110) and (220) crystal planes of the tetragonal structure of the $MAPbI_3$ perovskite phase. Similar peaks have previously been observed at 2θ = 14.1 and 28.42°, which correspond to q values of 1.0 and 2.0 Å^{-1}, respectively.[4,39,40] Our results agree with those of Yang et al., who studied the competition between different halides, concluding that irrespective of the ratio in which halides are present, the iodide dominates the final crystal structure after annealing with chloride only residing in small quantities at the grain boundaries,[6] and Pool et al., who used X-ray absorption near-edge structure to find that any remaining Cl present is at the grain boundaries or in poorly crystalline material.[41] The band gap of $MAPbI_3$ is known to be 1.6 eV, which is consistent with our UV−vis data for the final perovskite formed (not shown). This indicates that chloride is not substantially present in our final film, as does our WAXS data, which indicates that the final structure is $MAPbI_3$.

In the 1D radically integrated WAXS profiles of the annealed perovskite film shown in Figure 5, a very weak scattering peak at q = 1.1 Å^{-1} is still observed, which indicates the existence of a small amount of residual precursor product remains as an impurity. As in the previous section, scattering features
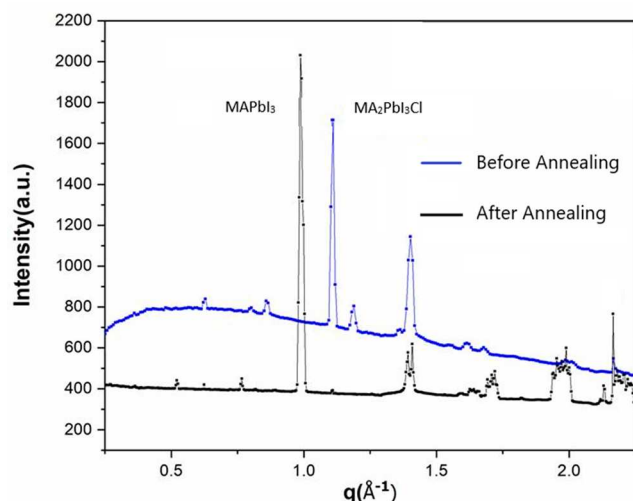
Figure 5. Comparison between the 1D radially integrated WAXS profiles of MA_2PbI_3Cl as-cast by spin coating and the resulting $MAPbI_3$ after thermal annealing at 90 °C for 2 h.

attributed to the mica substrate and excess MAI is observed at $q = 1.4$ and 2.16 $Å^{-1}$. This implies that both the stoichiometry of the mixture used and the annealing conditions used could both be further optimized so as to minimize these undesirable impurities within the films.

3c. *In Situ* Spin Coating of the 3:1 FAI:$PbCl_2$ Solution. The crystallization dynamics of $FAPbI_{3-x}Cl_x$ during the spin coating were also investigated using the same *in situ* WAXS technique. Figure 6 shows the time dependent radially
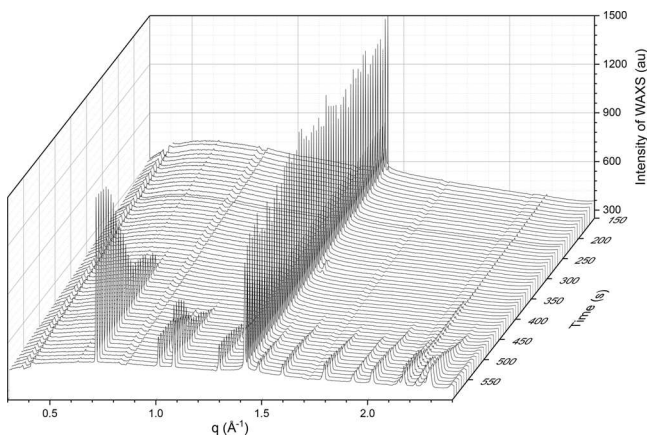

Figure 6. 1D integrated radial profile of the WAXS generated during the spin-casting of $FAPbI_{3-x}Cl_x$ solution plotted as a function of time.

integrated WAXS scattering profiles collected *in situ* as a function of processing time during spin-casting of the solution for $FAPbI_{3-x}Cl_x$. Initially, the only dominant sharp peak is observed at $q = 1.4$ $Å^{-1}$, which is attributed to scattering from the mica substrates as discussed previously. During the first 380 s, the broad solvent related feature present between 0.4 and 1.2 $Å^{-1}$ steadily disappears in the same way the solvent feature disappeared in Figure 2. This reduction in solvent scattering proceeds during the spin coating process. It is assumed that this scatter originates from the solvent originally as a liquid film and then trapped within the perovskite film, due to its persistence long after the film has solidified, reducing significantly after annealing.

As the film drying continues, other sharp peaks appear. Once the solvent has largely evaporated, evidence of crystallization is noted. After about 380 s, the yellow δ-$FAPbI_3$ phase forms, as revealed by the strong peak at $q = 0.7$ $Å^{-1}$. The initial stage of crystallization of δ-$FAPbI_3$ takes significantly longer to initiate than the formation of the first crystals observed when the casting solution for $MAPbI_3$ was used, where the initial appearance of crystalline peaks took only about 210 s. The WAXS peaks at 0.7, 1.3, 1.6, 1.8, and 2.3 $Å^{-1}$ are also attributed to the presence of the hexagonal structure of yellow-perovskite phase of δ-$FAPbI_3$, as was reported in X-ray diffraction results using a Cu Kα X-ray radiation source with $\lambda = 1.54$ Å in refs 42−44. Their appearance and the gradual enhancement of the associated WAXS intensity over time indicate that these peaks are related to crystals that are growing on the substrate as the solvent evaporates over time.

The WAXS signal at 1.1 $Å^{-1}$ is attributed to scattering caused by the intermediate product FACl; 1.1 $Å^{-1}$ is equivalent to an X-ray diffraction angle of 15.3° (for Cu Kα), where a diffraction peak from FACl has been reported.[22] This peak is not quite as intense as that associated with the yellow phase δ-$FAPbI_3$ at 0.7 $Å^{-1}$, and it is also noted that the crystallization mechanism for FACl takes longer to initiate (~440 s) as compared to 380 s for the δ-$FAPbI_3$ feature. At the same time as the appearance of the FACl peak, other new peaks associated with the perovskite phase of $FAPbI_{3-x}Cl_x$ are also detected at $q = 1.0$ and $q = 2.0$ $Å^{-1}$. These features occur at q values equivalent to the Bragg diffraction angles of 14.5 and 28° previously reported for $FAPbI_{3-x}Cl_x$ and show negligible difference to the X-ray diffraction from $FAPbI_3$.[22,44] Therefore, it is likely that the final films are $FAPbI_3$, but because some uncertainty remains, we continue to represent the FA perovskite films as $FAPbI_{3-x}Cl_x$. Finally, there is a period of stability where the sample does not change much. Lv et al.[22] describe the overall process as shown below as eq 4.[22]

$$3FAI + PbCl_2 \rightarrow FAPbI_{(3-x)}Cl_x + 2FACl \tag{4}$$
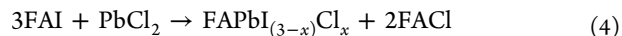
The dynamics of the crystallization processes involved in the preparation of $FAPbI_{3-x}Cl_x$ is not as straightforward as that for the $MAPbI_3$-casting as illustrated in Figure 7. It cannot be easily divided into three stages based on the *in situ* WAXS data presented. Initially, there is the same reduction in the background scattering due to the solvent evaporating as is the case when casting $MAPbI_3$. However, the subsequent process is more complex. The crystallization associated with the hexagonal yellow δ-$FAPbI_3$ precursor forming commences from 380 s onward. This is followed by the crystallization of FACl, which appears slightly later in the process after about 440 s, and at the same time, lower intensity peaks (compared to the δ-$FAPbI_3$) of the desired tetragonal perovskite $FAPbI_{3-x}Cl_x$ crystals are detected at $q = 1.0$ and 2.0 $Å^{-1}$. In this case, there are four stages during the crystal formation: solvent loss, initial δ-$FAPbI_3$ formation, the FACl and $FAPbI_{3-x}Cl$ crystallization, and finally a period of stability. Also, it should be noted that some of the desired perovskite phase $FAPbI_{3-x}Cl_x$ is formed directly without the requirement for annealing. This is in contrast to the spin coating of $MAPbI_3$ film, where only crystals of intermediate products were formed in the as-cast film. To produce $MAPbI_3$ films, annealing is required. There are three stages in the $MAPbI_3$ film-casting process and four in the $FAPbI_{3-x}Cl_x$ process, because there is an extra stage associated with the formation of the FACl and some of the desired $FAPbI_{3-x}Cl_x$ perovskite.

(a)   (b)
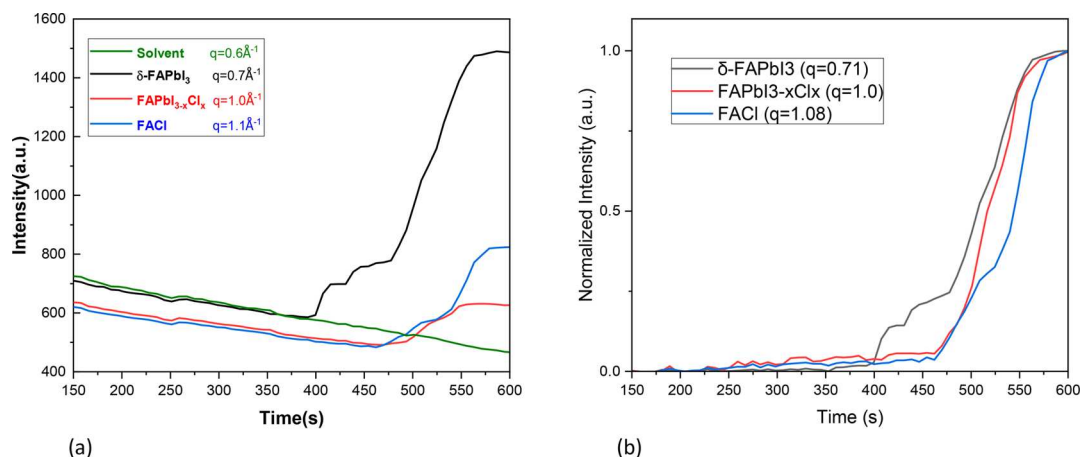
Figure 7. Peak intensity of the main WAXS features as they appear during the *in situ* observation of FAPbI$_{3-x}$Cl$_x$ perovskite film formation as a function of the time. Part (a) is the peak intensity as measured, and part (b) is the same data set after normalization and correction for the reduction in the solvent background over time. The peak intensity of the solvent background scattering was taken at $q = 0.6$ Å^{-1}, the δ-phase was taken at $q = 0.7$ Å^{-1}, the intermediate product of FACl was taken at $q = 1.1$ Å^{-1}, and the perovskite phase FAPbI$_{3-x}$Cl$_x$ was taken at $q = 1.0$ Å^{-1}.

The quality of the Avrami fits presented in Figure 8 are not as good as those for the MA$_2$PbI$_3$Cl film crystallization
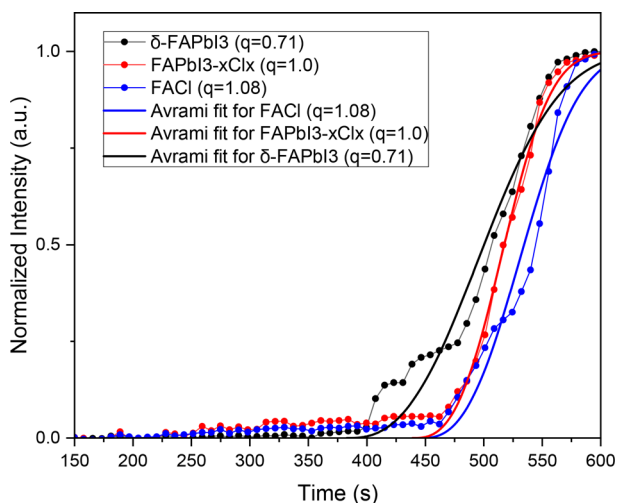
Figure 8. Avrami fitting applied to the WAXS peak intensity data for the formation of δ-FAPbI$_3$ at $q = 0.71$ Å^{-1}, FAPbI$_{3-x}$Cl$_x$ at $q = 1.0$ Å^{-1}, and FACl at $q = 1.08$ Å^{-1}. The Avrami exponent n was found to be 2.63 ± 1.23, 2.86 ± 0.97, and 2.67 ± 1.64 for the δ-FAPbI$_3$, FAPbI$_{3-x}$Cl$_x$, and FACl, respectively. Further details are shown in Figure S2.

presented as discussed in Figure 4, and as a result, the error associated with the exponent n is much larger here. It appears that the dimensionality of all the features presented here is of higher dimension than the features present in the MA system. The higher value of n suggests that the growth of the crystals in this case is more likely to be 3D. The δ-FAPbI$_3$ is known to have a 3D hexagonal structure.[42] The time at which crystallization begins is considerably later in the FA system, and it is noted that unlike the MA system, not all the materials that form here begin to crystallize at the same time. This could be because there are two crystallization processes competing for material as it falls out of solution due to solvent loss. The fitted start time for the δ-FAPbI$_3$ is at $t_0 = 382 ± 36$ s, but this process slows once the FACl and features FAPbI$_{3-x}$Cl$_x$ begin to appear after $t_0 = 446 ± 39$ s and $t_0 = 439 ± 19$ s,

respectively. This suggests that there is then competition for material falling out of solution and the appearance of the other materials slows down the further formation of the δ-FAPbI$_3$. Some of the material that would have formed δ-FAPbI$_3$ early in the process is now forming FACl, and we speculate that this results in strain induced conversion of some of the δ-FAPbI$_3$ into the desired FAPbI$_{3-x}$Cl$_x$.

3d. WAXS from the FAPbI$_{3-x}$Cl$_x$ Film upon Annealing. While some FAPbI$_{3-x}$Cl$_x$ is formed directly, in order to complete the conversion of the other precursor materials into FAPbI$_{3-x}$Cl$_x$, annealing is required. The main differences between the WAXS profiles of before and after annealing are presented in Figure 9(a). After annealing, high-intensity X-ray scattering peaks are observed at $q = 1.0$ Å^{-1} and $q = 2.0$ Å^{-1} associated with FAPbI$_{3-x}$Cl$_x$. In addition, there are several weak scattering peaks between 0.8 and 0.9 Å^{-1} that are attributed to PbI$_2$ and the peak at 1.4 Å^{-1}, which originates from the substrate and PbCl$_2$.[45] However, the group of scattering peaks associated with the hexagonal structure of δ-
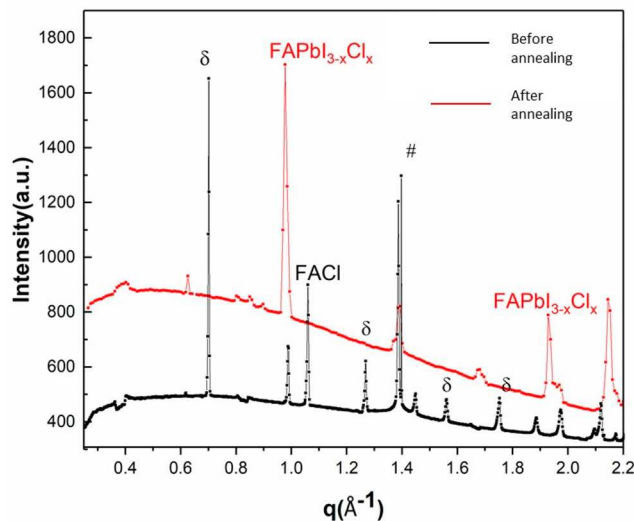
Figure 9. WAXS profiles of FAPbI$_{3-x}$Cl$_x$ films as-cast and after thermal annealing. The peaks associated with the δ-FAPbI$_3$ are labeled with a δ, and the # indicated the MAI and PbCl$_2$.

$FAPbI_3$ and the intermediate phase of FACl are no longer present. This indicates that they have undergone conversion into the desired $FAPbI_{3-x}Cl_x$ or evaporated.

The strong scattering peak around $q = 1.0$ A^{-1} is assigned to perovskite phase, as reported before.[22,46] The absence of the intermediate materials FACl and δ-FAPbI$_3$ indicate that the high-temperature annealing (190 °C) causes the conversion, decomposition, or evaporation of these intermediate products. The need for this higher temperature annealing to assist the complete formation of the $FAPbI_{3-x}Cl_x$ perovskite phase is associated with the phase transition at about 150 °C from the hexagonal δ-FAPbI$_3$ to the desired cubic perovskite phase.[47] However, it is noted that some $FAPbI_{3-x}Cl_x$ is formed without annealing and is present in the as-cast sample, as indicated by the weak scattering in the as-cast WAXS profile in Figure 9(a) at $q = 1.0$ Å^{-1} and $q = 2.0$ Å^{-1}. This may be due to FAPbI$_3$ being extremely sensitive to pressure[47] and the strain induced by the continually decreasing space and FACl crystallization within the drying film providing sufficient pressure to induce the desire phase transition in some of the FAPbI$_3$.

4. CONCLUSION

In situ WAXS has been used to follow the crystallization dynamics during the formation of MA and FA perovskite films. During spin-casting of the 3:1 MAI:PbCl$_2$ ink for MAPbI$_3$ fabrication at room temperature, the main crystals detected after the solvent has dried are consistent with the formation of a precursor MA_2PbI_3Cl with a 1D structure as described by Stone et al.,[8] which serves as an intermediate before the final perovskite phase forms upon annealing. The thermally unstable MA_2PbI_3Cl crystals are almost entirely converted into the final perovskite.

Significantly different dynamics were noted during the spin-casting of the $FAPbI_{3-x}Cl_x$ ink. First, the crystallization process is notably slower with the first intermediate products first detected more than 380 s after the start of the casting process, whereas the first crystals formed during $MAPbI_{3-x}Cl_x$ ink-casting after 210 s. Second, the yellow δ-FAPbI$_3$ phase crystallizes out of solution first, then after 440 s, there appears to be competition for the material falling out of solution between forming δ-FAPbI$_3$ or FACl, which is coincident with a small amount of the perovskite $FAPbI_{3-x}Cl_x$ forming. These two perovskites are known to have very different stabilities.[48] We propose that the enhanced stability of the FAPbI$_3$ is associated with its slower crystallization kinetics. The *in situ* WAXS data collected during spin-casting indicates that the $FAPbI_{3-x}Cl_x$ perovskite ink, which forms more slowly via a 3D precursor, is more stable, since some of the desired perovskite phase is formed directly, whereas $MAPbI_{3-x}Cl_x$ crystals form via a more rapidly crystallizing 1D precursor and only fully form after thermal annealing. These results suggest that there is potential to control the stability, morphology, and therefore device performance of perovskite materials through careful control of the film formation dynamics and could have a significant impact upon the lifetime for solar cells based on these perovskites.

ASSOCIATED CONTENT

SI **Supporting Information**

The Supporting Information is available free of charge at https://pubs.acs.org/doi/10.1021/acsaem.9b02470.

WAXS data for a clean substrate and $MAPbI_{3-x}Cl_x$ spin-cast at high and low speed; details of the Avrami fitting for $MAPbI_{3-x}Cl_x$; 2D WAXS images and SEM images from $MAPbI_{3-x}Cl_x$ before and after thermal annealing; details of the Avrami fitting for $FAPbI_{3-x}Cl_x$; 2D WAXS images from $FAPbI_{3-x}Cl_x$ before and after thermal annealing (PDF)

AUTHOR INFORMATION

Corresponding Author

Alan D. F. Dunbar − *Chemical and Biological Engineering, University of Sheffield, Sheffield S1 3JD, U.K.;* orcid.org/0000-0002-2313-4234; Email: a.dunbar@sheffield.ac.uk

Authors

Noura Alhazmi − *Chemical and Biological Engineering, University of Sheffield, Sheffield S1 3JD, U.K.*
Edwin Pineda − *Chemical and Biological Engineering, University of Sheffield, Sheffield S1 3JD, U.K.;* orcid.org/0000-0003-0508-3573
Jonathan Rawle − *Diamond Light Source, Didcot OX11 0DE, U.K.*
Jonathan R. Howse − *Chemical and Biological Engineering, University of Sheffield, Sheffield S1 3JD, U.K.*

Complete contact information is available at:
https://pubs.acs.org/10.1021/acsaem.9b02470

Notes

The authors declare no competing financial interest.

REFERENCES

(1) Alsari, M.; Bikondoa, O.; Bishop, J.; Abdi-Jalebi, M.; Ozer, L. Y.; Hampton, M.; Thompson, P.; Hörantner, M. T.; Mahesh, S.; Greenland, C.; Macdonald, J. E.; Palmisano, G.; Snaith, H. J.; Lidzey, D. G.; Stranks, S. D.; Friend, R. H.; Lilliu, S. In Situ Simultaneous Photovoltaic and Structural Evolution of Perovskite Solar Cells During Film Formation. *Energy Environ. Sci.* **2018**, *11* (2), 383−393.

(2) Kojima, A.; Teshima, K.; Shirai, Y.; Miyasaka, T. Organometal Halide Perovskites as Visible-Light Sensitizers for Photovoltaic Cells. *J. Am. Chem. Soc.* **2009**, *131* (17), 6050−6051.

(3) NREL. https://www.nrel.gov/pv/assets/pdfs/best-research-cell-efficiencies.20200406.pdf. 2017.

(4) Liu, M.; Johnston, M. B.; Snaith, H. J. Efficient planar heterojunction perovskite solar cells by vapour deposition. *Nature* **2013**, *501* (7467), 395−398.

(5) Conings, B.; Baeten, L.; De Dobbelaere, C.; D'Haen, J.; Manca, J.; Boyen, H.-G. Perovskite-Based Hybrid Solar Cells Exceeding 10% Efficiency with High Reproducibility Using a Thin Film Sandwich Approach. *Adv. Mater.* **2014**, *26* (13), 2041−2046.

(6) Yang, B.; Keum, J.; Ovchinnikova, O. S.; Belianinov, A.; Chen, S.; Du, M.-H.; Ivanov, I. N.; Rouleau, C. M.; Geohegan, D. B.; Xiao, K. Deciphering Halogen Competition in Organometallic Halide Perovskite Growth. *J. Am. Chem. Soc.* **2016**, *138* (15), 5028−5035.

(7) Munir, R.; Sheikh, A. D.; Abdelsamie, M.; Hu, H.; Yu, L.; Zhao, K.; Kim, T.; Tall, O. E.; Li, R.; Smilgies, D.-M.; Amassian, A. Hybrid Perovskite Thin-Film Photovoltaics: In Situ Diagnostics and Importance of the Precursor Solvate Phases. *Adv. Mater.* **2017**, *29* (2), 1604113.

(8) Stone, K. H.; Gold-Parker, A.; Pool, V. L.; Unger, E. L.; Bowring, A. R.; McGehee, M. D.; Toney, M. F.; Tassone, C. J. Transformation from Crystalline Precursor to Perovskite in PbCl$_2$-derived MAPbI$_3$. *Nat. Commun.* **2018**, *9* (1), 3458.

(9) Stranks, S. D.; Eperon, G. E.; Grancini, G.; Menelaou, C.; Alcocer, M. J. P.; Leijtens, T.; Herz, L. M.; Petrozza, A.; Snaith, H. J. Electron-Hole Diffusion Lengths Exceeding 1 Micrometer in an Organometal Trihalide Perovskite Absorber. *Science* **2013**, *342* (6156), 341−344.

(10) Tress, W. Perovskite Solar Cells on the Way to Their Radiative Efficiency Limit − Insights Into a Success Story of High Open-Circuit Voltage and Low Recombination. *Adv. Energy Mater.* **2017**, *7* (14), 1602358.

(11) Tidhar, Y.; Edri, E.; Weissman, H.; Zohar, D.; Hodes, G.; Cahen, D.; Rybtchinski, B.; Kirmayer, S. Crystallization of Methyl Ammonium Lead Halide Perovskites: Implications for Photovoltaic Applications. *J. Am. Chem. Soc.* **2014**, *136* (38), 13249−13256.

(12) Moore, D. T.; Sai, H.; Tan, K. W.; Smilgies, D.-M.; Zhang, W.; Snaith, H. J.; Wiesner, U.; Estroff, L. A. Crystallization Kinetics of Organic−Inorganic Trihalide Perovskites and the Role of the Lead Anion in Crystal Growth. *J. Am. Chem. Soc.* **2015**, *137* (6), 2350−2358.

(13) Chang, C.-Y.; Huang, Y.-C.; Tsao, C.-S.; Su, W.-F. Formation Mechanism and Control of Perovskite Films from Solution to Crystalline Phase Studied by in Situ Synchrotron Scattering. *ACS Appl. Mater. Interfaces* **2016**, *8* (40), 26712−26721.

(14) Barrows, A. T.; Lilliu, S.; Pearson, A. J.; Babonneau, D.; Dunbar, A. D.; Lidzey, D. G. Monitoring the Formation of a CH$_3$NH$_3$PbI$_{3-x}$Cl$_x$ Perovskite during Thermal Annealing Using X-Ray Scattering. *Adv. Funct. Mater.* **2016**, *26* (27), 4934−4942.

(15) Tan, K. W.; Moore, D. T.; Saliba, M.; Sai, H.; Estroff, L. A.; Hanrath, T.; Snaith, H. J.; Wiesner, U. Thermally Induced Structural Evolution and Performance of Mesoporous Block Copolymer-Directed Alumina Perovskite Solar Cells. *ACS Nano* **2014**, *8* (5), 4730−4739.

(16) Moore, D. T.; Sai, H.; Tan, K. W.; Smilgies, D.-M.; Zhang, W.; Snaith, H. J.; Wiesner, U.; Estroff, L. A. Crystallization Kinetics of Organic−Inorganic Trihalide Perovskites and the Role of the Lead Anion in Crystal Growth. *J. Am. Chem. Soc.* **2015**, *137* (6), 2350−2358.

(17) Lilliu, S.; Griffin, J.; Barrows, A. T.; Alsari, M.; Curzadd, B.; Dane, T. G.; Bikondoa, O.; Macdonald, J. E.; Lidzey, D. G. Grain Rotation and Lattice Deformation during Perovskite Spray Coating and Annealing Probed In Situ by GI-WAXS. *CrystEngComm* **2016**, *18* (29), 5448−5455.

(18) Pool, V. L.; Dou, B.; Van Campen, D. G.; Klein-Stockert, T. R.; Barnes, F. S.; Shaheen, S. E.; Ahmad, M. I.; van Hest, M. F. A. M.; Toney, M. F. Thermal engineering of FAPbI3 perovskite material via radiative thermal annealing and in situ XRD. *Nat. Commun.* **2017**, *8* (1), 14075.

(19) Yu, H.; Wang, F.; Xie, F.; Li, W.; Chen, J.; Zhao, N. The Role of Chlorine in the Formation Process of "CH3NH3PbI3-xClx" Perovskite. *Adv. Funct. Mater.* **2014**, *24* (45), 7102−7108.

(20) Colella, S.; Mosconi, E.; Fedeli, P.; Listorti, A.; Rizzo, A.; Gazza, F.; Orlandi, F.; Ferro, P.; Besagni, T.; Calestani, G. MAPbI$_{3-x}$Cl$_x$ Mixed Halide Perovskite for Hybrid Solar Cells: The Role of Chloride as Dopant on the Transport and StructuralProperties. *MRS Online Proc. Libr.* **2014**, *1667*, Mrss14-1667-b03-02.

(21) Colella, S.; Mosconi, E.; Fedeli, P.; Listorti, A.; Gazza, F.; Orlandi, F.; Ferro, P.; Besagni, T.; Rizzo, A.; Calestani, G.; Gigli, G.; De Angelis, F.; Mosca, R. MAPbI3-xClx Mixed Halide Perovskite for Hybrid Solar Cells: The Role of Chloride as Dopant on the Transport and Structural Properties. *Chem. Mater.* **2013**, *25* (22), 4613−4618.

(22) Lv, S.; Pang, S.; Zhou, Y.; Padture, N. P.; Hu, H.; Wang, L.; Zhou, X.; Zhu, H.; Zhang, L.; Huang, C.; et al. One-step, Solution-Processed Formamidinium Lead Trihalide (FAPbI(3− x) Clx) for Mesoscopic Perovskite−Polymer Solar Cells. *Phys. Chem. Chem. Phys.* **2014**, *16* (36), 19206−19211.

(23) Chen, C.-Y.; Lin, H.-Y.; Chiang, K.-M.; Tsai, W.-L.; Huang, Y.-C.; Tsao, C.-S.; Lin, H.-W. All-Vacuum-Deposited Stoichiometrically Balanced Inorganic Cesium Lead Halide Perovskite Solar Cells with Stabilized Efficiency Exceeding 11%. *Adv. Mater.* **2017**, *29* (12), 1605290.

(24) Lin, H.-Y.; Chen, C.-Y.; Hsu, B.-W.; Cheng, Y.-L.; Tsai, W.-L.; Huang, Y.-C.; Tsao, C.-S.; Lin, H.-W. Efficient Cesium Lead Halide Perovskite Solar Cells through Alternative Thousand-Layer Rapid Deposition. *Adv. Funct. Mater.* **2019**, *29* (44), 1905163.

(25) *Dawn Science Home Page.* https://dawnsci.org/.

(26) Tan, K. W.; Moore, D. T.; Saliba, M.; Sai, H.; Estroff, L. A.; Hanrath, T.; Snaith, H. J.; Wiesner, U. Thermally Induced Structural Evolution and Performance of Mesoporous Block Copolymer-directed Alumina Perovskite Solar Cells. *ACS Nano* **2014**, *8*, 4730.

(27) Huang, Y.-C.; Tsao, C.-S.; Cho, Y.-J.; Chen, K.-C.; Chiang, K.-M.; Hsiao, S.-Y.; Chen, C.-W.; Su, C.-J.; Jeng, U.-S.; Lin, H.-W. Insight into Evolution, Processing and Performance of Multi-length-scale Structures in Planar Heterojunction Perovskite Solar Cells. *Sci. Rep.* **2015**, *5*, 13657.

(28) Unger, E. L.; Bowring, A. R.; Tassone, C. J.; Pool, V. L.; Gold-Parker, A.; Cheacharoen, R.; Stone, K. H.; Hoke, E. T.; Toney, M. F.; McGehee, M. D. Chloride in Lead Chloride-derived Organo-metal Halides for Perovskite-Absorber Solar Cells. *Chem. Mater.* **2014**, *26* (24), 7158−7165.

(29) Zhou, H.; Chen, Q.; Li, G.; Luo, S.; Song, T.-b.; Duan, H.-S.; Hong, Z.; You, J.; Liu, Y.; Yang, Y. Interface Engineering of Highly Efficient Perovskite Solar Cells. *Science* **2014**, *345* (6196), 542−546.

(30) Liu, J.; Gao, C.; He, X.; Ye, Q.; Ouyang, L.; Zhuang, D.; Liao, C.; Mei, J.; Lau, W. Improved Crystallization of Perovskite Films by Optimized Solvent Annealing for High Efficiency Solar Cell. *ACS Appl. Mater. Interfaces* **2015**, *7* (43), 24008−24015.

(31) Poglitsch, A.; Weber, D. Dynamic Disorder in Methylammoniumtrihalogenoplumbates (II) Observed by Millimeter-wave Spectroscopy. *J. Chem. Phys.* **1987**, *87* (11), 6373−6378.

(32) Mosconi, E.; Amat, A.; Nazeeruddin, M. K.; Grätzel, M.; De Angelis, F. First-Principles Modeling of Mixed Halide Organometal Perovskites for Photovoltaic Applications. *J. Phys. Chem. C* **2013**, *117* (27), 13902−13913.

(33) Jeon, N. J.; Noh, J. H.; Kim, Y. C.; Yang, W. S.; Ryu, S.; Seok, S. I. Solvent Engineering for High-performance Inorganic−organic Hybrid Perovskite Solar Cells. *Nat. Mater.* **2014**, *13* (9), 897−903.

(34) Toolan, D. T. W.; Isakova, A.; Hodgkinson, R.; Reeves-McLaren, N.; Hammond, O. S.; Edler, K. J.; Briscoe, W. H.; Arnold, T.; Gough, T.; Topham, P. D.; Howse, J. R. Insights into the Influence of Solvent Polarity on the Crystallization of Poly(ethylene oxide) Spin-Coated Thin Films via in Situ Grazing Incidence Wide-Angle X-ray Scattering. *Macromolecules* **2016**, *49* (12), 4579−4586.

(35) Wu, W.-R.; Su, C.-J.; Chuang, W.-T.; Huang, Y.-C.; Yang, P.-W.; Lin, P.-C.; Chen, C.-Y.; Yang, T.-Y.; Su, A.-C.; Wei, K.-H.; Liu, C.-M.; Jeng, U.-S. Surface Layering and Supersaturation for Top-Down Nanostructural Development during Spin Coating of Polymer/Fullerene Thin Films. *Adv. Energy Mater.* **2017**, *7* (14), 1601842.

(36) Fanfoni, M.; Tomellini, M. The Johnson-Mehl- Avrami-Kohnogorov Model: A Brief Review. *Nuovo Cimento Soc. Ital. Fis., D* **1998**, *20* (7), 1171−1182.

(37) Avrami, M. Kinetics of Phase Change. I General Theory. *J. Chem. Phys.* **1939**, *7* (12), 1103−1112.

(38) Jena, A. K.; Chaturvedi, M. C. *Phase transformation in materials*; Prentice Hall, 1991.

(39) Wang, Z. K.; Li, M.; Yang, Y. G.; Hu, Y.; Ma, H.; Gao, X. Y.; Liao, L. S. High Efficiency Pb−In Binary Metal Perovskite Solar Cells. *Adv. Mater.* **2016**, *28* (31), 6695−6703.

(40) Miyadera, T.; Shibata, Y.; Koganezawa, T.; Murakami, T. N.; Sugita, T.; Tanigaki, N.; Chikamatsu, M. Crystallization Dynamics of Organolead Halide Perovskite by Real-Time X-ray Diffraction. *Nano Lett.* **2015**, *15* (8), 5630−5634.

(41) Pool, V. L.; Gold-Parker, A.; McGehee, M. D.; Toney, M. F. Chlorine in PbCl$_2$-Derived Hybrid-Perovskite Solar Absorbers. *Chem. Mater.* **2015**, *27* (21), 7240−7243.

(42) Aguiar, J. A.; Wozny, S.; Holesinger, T. G.; Aoki, T.; Patel, M. K.; Yang, M.; Berry, J. J.; Al-Jassim, M.; Zhou, W.; Zhu, K. In Situ Investigation of the Formation and Metastability of Formamidinium Lead Tri-iodide Perovskite Solar Cells. *Energy Environ. Sci.* **2016**, *9* (7), 2372−2382.

(43) Stoumpos, C. C.; Malliakas, C. D.; Kanatzidis, M. G. Semiconducting Tin and Lead Iodide Perovskites with Organic Cations: Phase Transitions, High Mobilities, and Near-infrared Photoluminescent Properties. *Inorg. Chem.* **2013**, *52* (15), 9019−9038.

(44) Numata, Y.; Sanehira, Y.; Miyasaka, T. Impacts of Heterogeneous TiO_2 and Al_2O_3 Composite Mesoporous Scaffold on Formamidinium Lead Trihalide Perovskite Solar Cells. *ACS Appl. Mater. Interfaces* **2016**, *8* (7), 4608−4615.

(45) Chen, S.; Chen, B.; Gao, X.; Dong, B.; Hu, H.; Yan, K.; Wen, W.; Zou, D. Neutral-colored Semitransparent Solar Cells Based on Pseudohalide (SCN−)-Doped Perovskite. *Sustainable Energy Fuels* **2017**, *1* (5), 1034−1040.

(46) Yuan, D.-X.; Gorka, A.; Xu, M.-F.; Wang, Z.-K.; Liao, L.-S. Inverted Planar $NH_2CH = NH_2PbI_3$ Perovskite Solar Cells with 13.56% Efficiency via Low Temperature Processing. *Phys. Chem. Chem. Phys.* **2015**, *17* (30), 19745−19750.

(47) Jiang, S.; Luan, Y.; Jang, J. I.; Baikie, T.; Huang, X.; Li, R.; Saouma, F. O.; Wang, Z.; White, T. J.; Fang, J. Phase Transitions of Formamidinium Lead Iodide Perovskite under Pressure. *J. Am. Chem. Soc.* **2018**, *140* (42), 13952−13957.

(48) Fan, Y.; Meng, H.; Wang, L.; Pang, S. Review of Stability Enhancement for Formamidinium-Based Perovskites. *Sol. RRL* **2019**, *3*, 1900215.